Clays and Clay Minerals (2024), **72**, e15, 1–17
doi:10.1017/cmn.2024.27

Original Paper

Physico-chemical properties and microstructure of bentonite in highly alkaline environments

Achraf Harrou[1], Mahdi Lechheb[2], Meriam El Ouahabi[3], Nathalie Fagel[3] and Elkhadir Gharibi[1]

[1]Laboratory of Applied Chemistry and Environment Team of Mineral Solid Chemistry, Faculty of Sciences, Mohammed First University, Oujda, PO Box 60000, Morocco; [2]Materials Sciences for Energy and Sustainable Development Team, Department of Chemistry, Faculty of Sciences and Techniques, Moulay Ismail University, Errachidia, Morocco and [3]Laboratory Argiles, Geochemistry and Sedimentary Environments (AGEs), Department of Geology, Quartier Agora, Sart-Tilman, University of Liège, B-4000, Belgium

Abstract

Cementitious materials and their alkaline pore fluids can change the structure of bentonite used as a raw material for road embankments or concrete storage of garbage cans. This study investigated the alteration of montmorillonite-rich bentonite from northeast Morocco (Trebia deposit, Nador) in alkaline media rich in Ca^{2+}, Mg^{2+}, Na^{+}, or K^{+}. Specimens based on raw bentonite mixed with variable proportions of oxides (CaO, MgO) or hydroxides (NaOH, KOH) and water were prepared and aged for 28 days. Mineralogical composition by X-ray diffraction (XRD) was determined on raw bentonite and specimens to follow phase changes. Chemical composition and thermal characteristics were determined for raw bentonite and specimens by Fourier-transform infrared spectroscopy (FT-IR) and thermogravimetric/differential thermal analysis (TGA/DTA). Microstructural evolution and alteration of the external surface of bentonite were evaluated using scanning electron microscopy coupled with energy dispersive X-ray (SEM/EDX) analysis. XRD results of bentonite-CaO mixture demonstrated the formation of gels (e.g. C-S-H) and calcite. When the amount of CaO added increased, excess portlandite and the precipitation of calcite in the outer surface of bentonite occurred, stopping pozzolanic reaction and consequently decreasing the compressive strength of specimens. On the other hand, the addition of MgO allowed the formation of brucite. Sodalite and cancrinite were neoformed with the addition of 32 wt.% NaOH after 28 days of hydration. The addition of hydroxides (NaOH or KOH) to bentonite did not reveal any setting due to the absence of the formation of cementitious phases.

Keywords: compressive strength; gel (C-S-H); hydration; smectite; sodalite

(Received: 22 February 2024; revised: 28 June 2024; accepted: 05 July 2024)

Introduction

Bentonite, often referring to a range of smectite minerals, is a widely available clay rock composed primarily of dioctahedral montmorillonite/beidellite (Christidis, 2011). Calcium montmorillonite is more comment than sodium montmorillonite worldwide (Murray, 2006). It is frequently used as an alkali-activated aluminosilicate in the production of geopolymer for construction materials, offering a more environmentally friendly alternative to traditional materials like Portland cement-based concrete (Provis, 2014; Khalifa et al., 2020). The stability of bentonite in alkaline conditions is a critical factor that influences its effectiveness in these applications.

Research has been conducted on the alkali activation of clays rich in smectite due to their abundance and cost effectiveness (MacKenzie, 2009; Marsh et al., 2019). Montmorillonites have two of their three octahedral sites filled predominantly by trivalent cations such as Al and Fe (Yan and Zhang, 2021). Their properties can be influenced by tetrahedral/octahedral substitutions: Al^{3+} substitutes for Si^{4+} in the tetrahedral sheet and Fe^{2+}/Mg^{2+} substitutes for Al^{3+} in the octahedral sheet (Murray, 2000). Isomorphic substitution with lower-valence cations for montmorillonite creates negative charges on the surface of the sheets. In the natural state, negative charges are compensated by exchangeable interlayer cations (Na^{+}, K^{+}, Ca^{2+}, Mg^{2+}) (Huang and Zhang, 2023). They are located in the interlayer space or on the external surface of the clay particles (Tsipursky and Drits, 1984).

When exposed to an alkaline solution, smectites undergo a corrosion process that is very dependent on pH, temperature, and the nature of the electrolytes in the solution (Asano et al., 2008; Xiang et al., 2019). Following corrosion in an alkaline solution, montmorillonite aggregates fracture into smaller stacks, and the surface of the montmorillonite layers becomes more uneven (Xiang et al., 2019). The swelling pressure of the homoionic smectites follows the trend $Mg^{2+}>Ca^{2+}>Sr^{2+}>Ba^{2+}$ (Fayoyiwa et al., 2020). The volume change resulting from interlayer hydration and dehydration in the crystalline swelling regime for

Corresponding authors: Achraf Harrou and Elkhadir Gharibi; Emails: Harrou201@gmail.com; gharibi_elkhadir@yahoo.fr

Cite this article: Harrou A., Lechheb M., El Ouahabi M., Fagel N., & Gharibi E. (2024). Physico-chemical properties and microstructure of bentonite in highly alkaline environments. *Clays and Clay Minerals* **72**, e15, 1–17. https://doi.org/10.1017/cmn.2024.27

Ca-montmorillonite is significantly greater than for Na-montmorillonite (Likos and Lu, 2006).

In alkaline lime solution (pH ~12), montmorillonite undergoes dissolution/precipitation affecting its structure (Oumnih et al., 2019; Harrou et al., 2020). However, exposure to $Mg(OH)_2$ does not alter the structure of montmorillonite, but leads to $Mg(OH)_2$ clusters forming in the interlayer spaces, preventing bentonite from swelling in water (El Bouraie and Masoud, 2017; Patel et al., 2006). Ammonia increases the permeability coefficient of the bentonite-clay mixture, alters its porosity and network, and decreases crystalline swelling (Gautier et al., 2010; Sun et al., 2021). The reaction of bentonite with CsOH produces pollucite, a zeolite mineral (Jing et al., 2016).

Solutions of NaOH and KOH allow the dissolution of bentonite, a process that increases with an increase in the concentration of the alkaline solution. The dissolution is more pronounced in NaOH solution (Xiang et al., 2022). NaOH or $Ca(OH)_2$ concentrated solutions transform Na-montmorillonite into Na-beidellite or Ca-montmorillonite (Asano et al., 2008). In hyperalkaline K-Na-OH-type solution (pH ≤13), a partial dissolution of bentonite occurs, leading to the precipitation of secondary phases (e.g. analcime, sanidine, orthoclase) and the formation of illite-smectite interstratified minerals (Fernández et al., 2014). In KOH solutions, from 80°C, a cementitious material was produced leading to the kaolinitization of bentonite and its partial transformation into kaolinite and pyrophyllite (Ye et al., 2016).

Despite the abundance of research on this topic, a few studies focused on soils containing Na- and Ca-montmorillonite along with other non-clay mineral phases. Note that montmorillonite is found in a wide variety of soils worldwide (Nickovic et al., 2012). However, the influence of secondary phases present in natural bentonites on the reactivity of montmorillonite in an alkaline environment is still unverified. This study aims to assess the reactivity of natural bentonite with oxides (CaO, MgO) or hydroxides (NaOH, KOH) and water. The bentonite studied is composed of Ca-montmorillonite and Na-montmorillonite with small amounts of Mg and K. Secondary phases, such as quartz and feldspars, are detected in the bentonite used. Likewise, the four cations present in the bases tested (Ca, Mg, Na, K) are also present as secondary phases in the bentonite. The only extrinsic parameter modified, in this study, was the pH established by each base added. The determination of the stability of bentonite with respect to each base will allow a more selective use of bentonite as a raw material in road embankments or in the concrete storage of garbage cans.

Materials and methods

Raw materials

The raw bentonite sample was collected from the Trebia deposit (N35°09′07″, W03°07′48″) located in the Nador region (Northeastern Morocco). The raw sample is composed of Ca-montmorillonite (Ca-Mt), Na-montmorillonite (Na-Mt), Na-feldspar (NaFs), K-feldspar (KFs) and anorthite (An) (Harrou et al., 2020). Chemically, the bentonite contains SiO_2 (50.2%) and Al_2O_3 (23.9%) with small amounts of CaO (1.33%), MgO (1.49%), Na_2O (1.32%), and K_2O (0.85%). From the point of view of particle size, the bentonite studied is composed of ~66% of clay fraction (<2 μm) (Table 1). Based on liquid limit and plastic limit values, this bentonite is classified as fatty clay of high plasticity according to the Unified Soil Classification System (USCS). The bentonite, in suspension in water for 30 min (solid/liquid ratio = 0.5), gives an alkaline solution with a pH ~9.

Table 1. Some properties of raw bentonite

Properties	
pH	8.72
Liquid limit (%)	103
Plastic limit (%)	30.5
Total specific surface area ($m^2\ g^{-1}$)	68–74 (Daou et al., 2015; Bounab et al., 2017)
Cation exchange capacity (mmol g^{-1})	84.7–88.9 (Daou et al., 2015; Bounab et al., 2017)
Mineral composition	Ca-montmorillonite (Ca-mt) Na-montmorillonite (Na-mt) Kaolinite (Kao) Na-feldspar (NaF) K-feldspar (KF) Anorthite (An)
Clay content (%)	66

The chemical reagents used, CaO, MgO, KOH, and NaOH, are of very high quality (PA 99.9%) and were purchased from Sigma-Aldrich (Oujda, Morocco).

Experimentation

A bentonite sample was crushed and sieved to 250 μm before being used. CaO and MgO samples were calcined at 1000°C for 4 h prior to use. A total of 16 solid mixtures were prepared from the raw bentonite and oxides (CaO or MgO) or hydroxides (NaOH or KOH) (Table 2). The mortar specimens were prepared by moistening the solid mixtures with distilled water; the liquid/solid

Table 2. The mass of raw bentonite and the adjuvants used to manufacture specimens

Code	Bentonite	$Ca(OH)_2$	$Mg(OH)_2$	NaOH	KOH	pH
	(wt.%)					
BC1	98	2	—	—	—	12.1
BC2	92	8	—	—	—	12.4
BC3	84	16	—	—	—	12.7
BC4	68	32	—	—	—	13.2
BM1	98	—	2	—	—	11.5
BM2	92	—	8	—	—	11.4
BM3	84	—	16	—	—	11.7
BM4	68	—	32	—	—	12.1
BN1	98	—	—	2	—	12.3
BN2	92	—	—	8	—	12.7
BN3	84	—	—	16	—	>14
BN4	68	—	—	32	—	>14
BK1	98	—	—	—	2	12.6
BK2	92	—	—	—	8	12.7
BK3	84	—	—	—	16	>14
BK4	68	—	—	—	32	>14

https://doi.org/10.1017/cmn.2024.27 Published online by Cambridge University Press

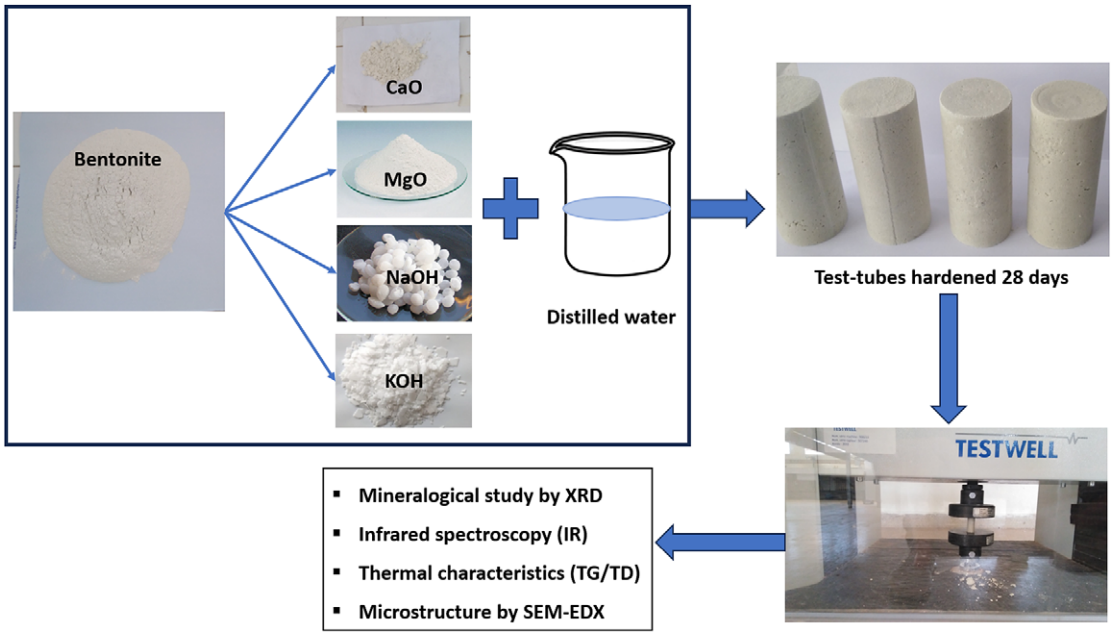

Figure 1. Experimental protocol.

ratio was 0.46 (Fig. 1). During the first minutes of mixing, a liquid phase covered the solid. The pH of the mixing solution was measured after 30 min of stirring and settling of the solid. The pH increased with the addition of the oxide (CaO or MgO) or hydroxide (NaOH or KOH) and followed the MgO < CaO < NaOH ≤ KOH trend. With the addition of MgO or CaO, the pH increased from 11.5 to 12, or from 12 to 13, respectively. When the amount of NaOH or KOH added was 16% or 32%, respectively, the pH exceeded the maximum value of pH meter (>14).

The specimens prepared were in the form of cylinders with a diameter of 3.2 cm, a height of 6.4 cm and an average weight of 8 g according to ASTM Standard D1621. Thereafter, the specimens were placed in a binder type E28 incubator for 28 days to harden at a constant temperature of 25°C.

Analytical methods

The mineralogical compositions of samples were assessed by means of X-ray diffraction (XRD) analysis using a Shimadzu 6100 diffractometer equipped with a CuKα radiation tube (λ=1.54 nm) in the range 2–70°2θ and a step size of 0.004°2θ (Chemistry Department, Faculty of Sciences, Oujda, Morocco). The specimens were ground and placed in XRD holders to determine their mineralogical composition. All samples were dried in the oven for 12 h before XRD analysis.

Fourier-transform infrared spectroscopy (FTIR) analysis was done using a Fourier-transform JASCO-FTIR-4700 spectrometer in attenuated total reflectance (ATR) mode, equipped with a DLaTGS detector and Peltier temperature control. A rapid 10 Hz scan with a resolution of 0.4 cm^{-1} was acquired in a wavelength range of 400–4000 cm^{-1} (Chemistry Department, Faculty of Sciences, Oujda, Morocco).

Thermogravimetric (TGA) and differential thermal analysis (DTA) was performed using a Shimadzu DTG-60 instrument (Chemistry Department, Faculty of Sciences, Oujda, Morocco). The samples were heated at a rate of 10°C min^{-1} from room temperature to 1000°C.

The morphology of hydrated specimens was studied at the National Centre for Scientific Research (CNRST, Rabat, Morocco), by scanning electron microscopy (SEM) coupled with energy dispersive X-ray spectroscopy (EDX) with QUANTA (resolution of 3.5 nm and 133 eV, detector: SE, BSE, LFD, and GBSE).

The compressive strength of hydrated specimens was determined used a TESTWELL device at a speed of 0.5 mm min^{-1}, according to ASTM Standard D1621 (Faculty of Sciences, Oujda, Morocco).

The follow-up of the evolution of the setting of the specimens after 28 days of hydration was performed using XRD, FTIR spectroscopy, TGA/TDA, and compressive strength. The SEM/EDS results were obtained after 90 days of hydration.

Results and Discussion

Mineralogical composition

The XRD pattern of bentonite mixed with small proportions of CaO (BC1 and BC3) showed characteristic peaks of Ca-montmorillonite, Na-montmorillonite, anorthite, K-feldspar, Na-feldspar, portlandite, calcite, and calcium silicate hydrate (C-S-H) (Fig. 2). The peak representing portlandite increased in intensity as the amount of lime added was increased. The peak at ~32.72 2θ (2.71 Å) appeared broader and less intense, probably due to the presence of C-S-H (Lothenbach et al., 2015).

A strong base, $Ca(OH)_2$, was obtained by hydration of CaO. The solubility product of $Ca(OH)_2$ is equal to Ksp 5×10^{-6} (Dodds et al., 2017). OH^- and Ca^{2+} ions were released into the intragranular solution of the bentonite aggregates. At pH >11 and in wet conditions, OH^- ions adsorbed to the surface of montmorillonite forming silanol (Si-OH) and aluminol (Al-OH) bonds. Ca^{2+} reacted with the tetrahedral silanol and octahedral aluminol to form the calcium silicate hydrate (C-S-H) and calcium alumino-silicate hydrate (C-S-A-H) gels. The tetrahedral silica evolves from a Q_3 to a Q_1 environment upon C-S-H formation

https://doi.org/10.1017/cmn.2024.27 Published online by Cambridge University Press

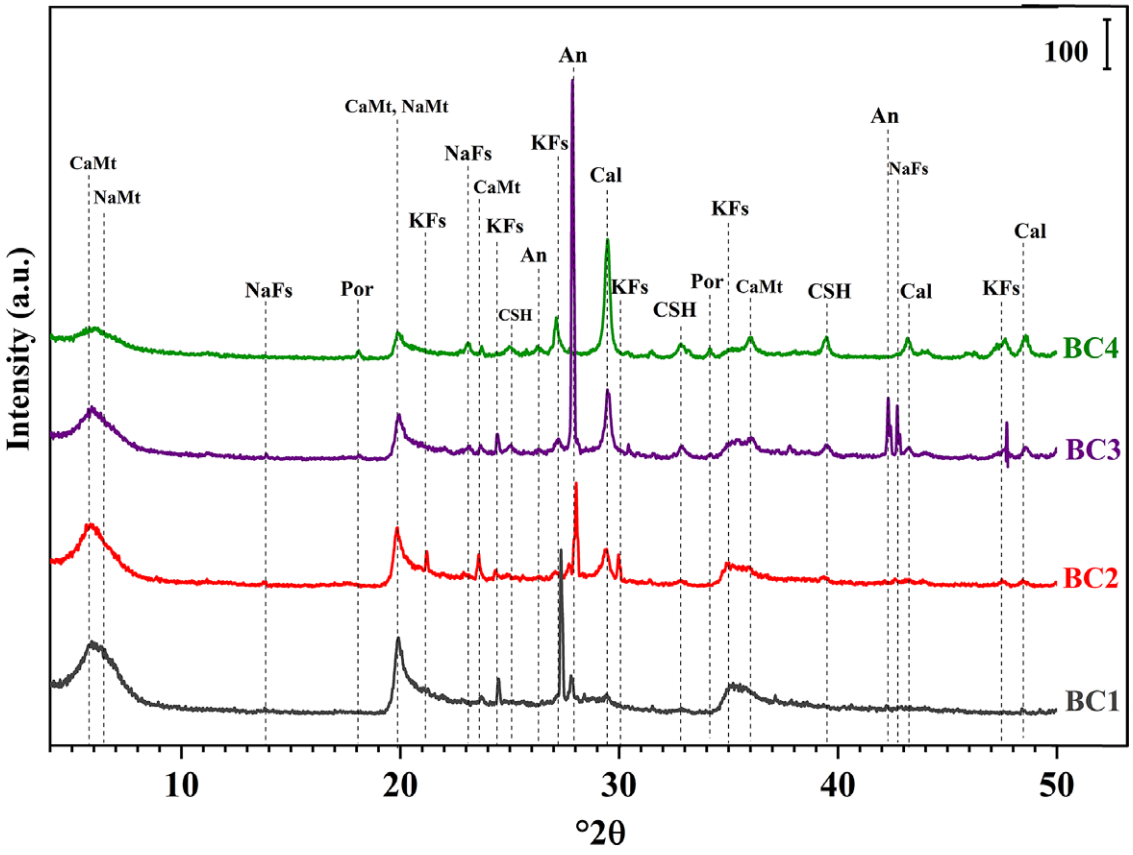

Figure 2. XRD pattern of bentonite mixed with variable amounts of CaO. CaMt = calcium montmorillonite; NaMt = sodium montmorillonite; An = anorthite; Cal = calcite; KFs = K-feldspar; NaFs = Na-feldspar; Por = portlandite; CSH = calcium silicate hydrate.

(Vitale et al., 2017). Calcite is formed by the carbonation reaction of lime in the presence of CO_2 according to the following reaction (Eqn 1):

$$CO_2 + Ca(OH)_2 \Leftrightarrow Ca^{2+} + CO_3^{2-} + H_2O \Leftrightarrow CaCO_3 + H_2O. \quad (1)$$

The precipitation of calcite on the surface of bentonite grains hinders the formation of C-S-H (Baldermann et al., 2019).

The XRD pattern of bentonite-magnesium hydroxide mixtures (Fig. 3) showed the presence of Ca-montmorillonite, Na-montmorillonite, kaolinite, anorthite, K-feldspar, Na-feldspar, brucite, and periclase. In the mixtures BM1, BM2, and BM3, periclase (MgO) was entirely consumed to give brucite ($Mg(OH)_2$). MgO persisted in the BM4 mixture. The brucite-forming reaction is slow (Eqn 2):

$$MgO + H_2O \rightarrow Mg^{2+} + 2OH^- \rightarrow Mg(OH)_2 \quad (2)$$

Likewise, the solubility product of brucite (Mg^{2+} and OH^-) is low with Ksp 2×10^{-13} (Dodds et al., 2017). The peak at 7.22 Å (12.21°2θ) could correspond to kaolinite of low crystallinity in raw bentonite.

The XRD pattern of bentonite-sodium hydroxide mixtures (Fig. 4) showed the presence of Ca-montmorillonite, Na-montmorillonite, anorthite, K-feldspar, Na-feldspar, sodalite, and cancrinite.

The addition of 16% of NaOH to the bentonite (BN3) allowed the transformation of the bentonite to Na-montmorillonite by substitution of one calcium by two sodium ions (Fig. 4). This is due to neighboring cationic radii of Na^+ and Ca^{2+}. The XRD pattern of the bentonite mixed with 32 wt.% of NaOH (BN4) showed the formation of sodalite ($Na_8(Al_6Si_6O_{24})(OH)_2(H_2O)_2$) and cancrinite ($Na_6Ca_2Al_6Si_6O_{24}(CO_3)_2.2H_2O$) (Fig. 4). The peak of montmorillonite disappeared, probably because of its dissolution in a highly sodium alkaline medium (pH >14). Pure hydroxysodalite can be formed from bentonite in the following conditions: (1) Na/Si molar ratio of 12; (2) Si/Al molar ratio of 1.0; (3) temperature of reaction of 90°C; (4) reaction time of 12 h (Liu et al., 2018). It can also occur after a long stay of montmorillonite in a solution of NaOH (Elert et al., 2015). Zeolite, as cancrinite formed in sample BN4, can be obtained after sodium attack of montmorillonite (Seo et al., 2018); its formation is favored by the CO_2 (Hackbarth et al., 1999).

In an aqueous and highly alkaline medium (pH >14), OH^- ions adsorb on montmorillonite to form Si-OH and Al-OH bonds. The excess sodium substitutes the proton and promotes the dissolution of the cancrinite to form metastable phases: Na_2SiO_3 and $NaAlO_2$. With time, sodalite is formed according to the following reaction (Eqn 3) (Zong et al., 2020):

$$6Na_2SiO_3 + 6NaAlO_2 + 8H_2O \rightarrow Na_8(Al_6Si_6O_{24})(OH)_2(H_2O)_2 + 10NaOH \quad (3)$$

The XRD pattern of bentonite-potassium hydroxide mixtures (Fig. 5) indicated the presence Ca-montmorillonite, Na-montmorillonite, kaolinite, anorthite, K-feldspar, Na-feldspar, hydrated potassium aluminum oxide, and potassium carbonate sesquihydrate.

https://doi.org/10.1017/cmn.2024.27 Published online by Cambridge University Press

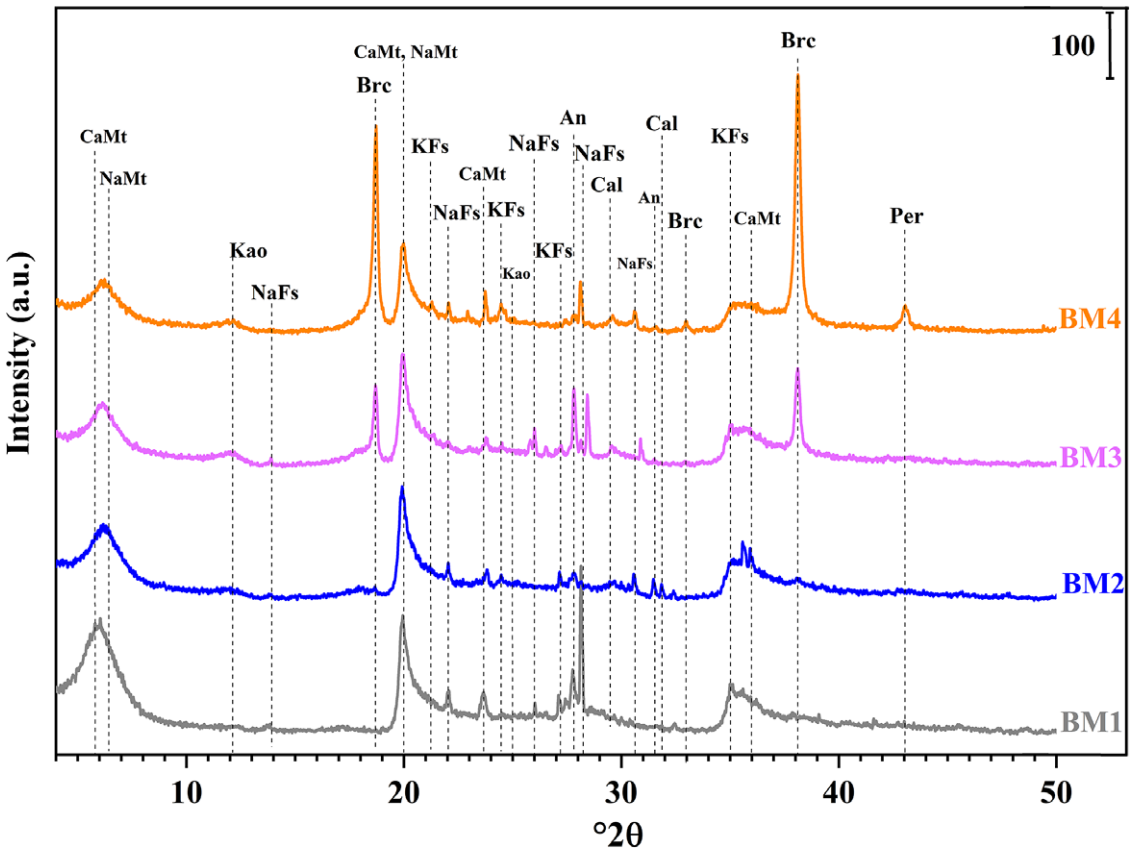

Figure 3. XRD patterns of BM1, BM2, BM3, and BM4 mixtures. CaMt = calcium montmorillonite; NaMt = sodium montmorillonite; An = anorthite; KFs = K-feldspar; NaFs = Na-feldspar; Brc = brucite; Per = periclase; Kao = kaolinite.

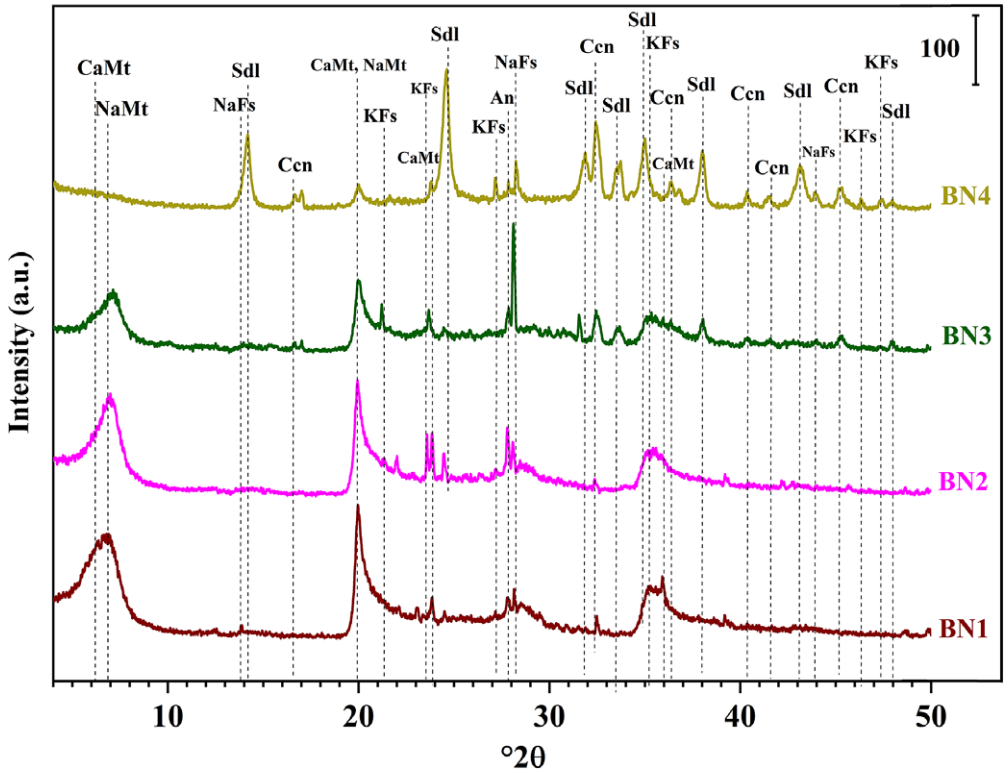

Figure 4. XRD pattern of BN1, BN2, BN3, and BN4 mixtures. CaMt = calcium montmorillonite; NaMt = sodium montmorillonite; An = anorthite; KFs = K-feldspar; NaFs = Na-feldspar; Sdl = sodalite; Ccn = cancrinite

https://doi.org/10.1017/cmn.2024.27 Published online by Cambridge University Press

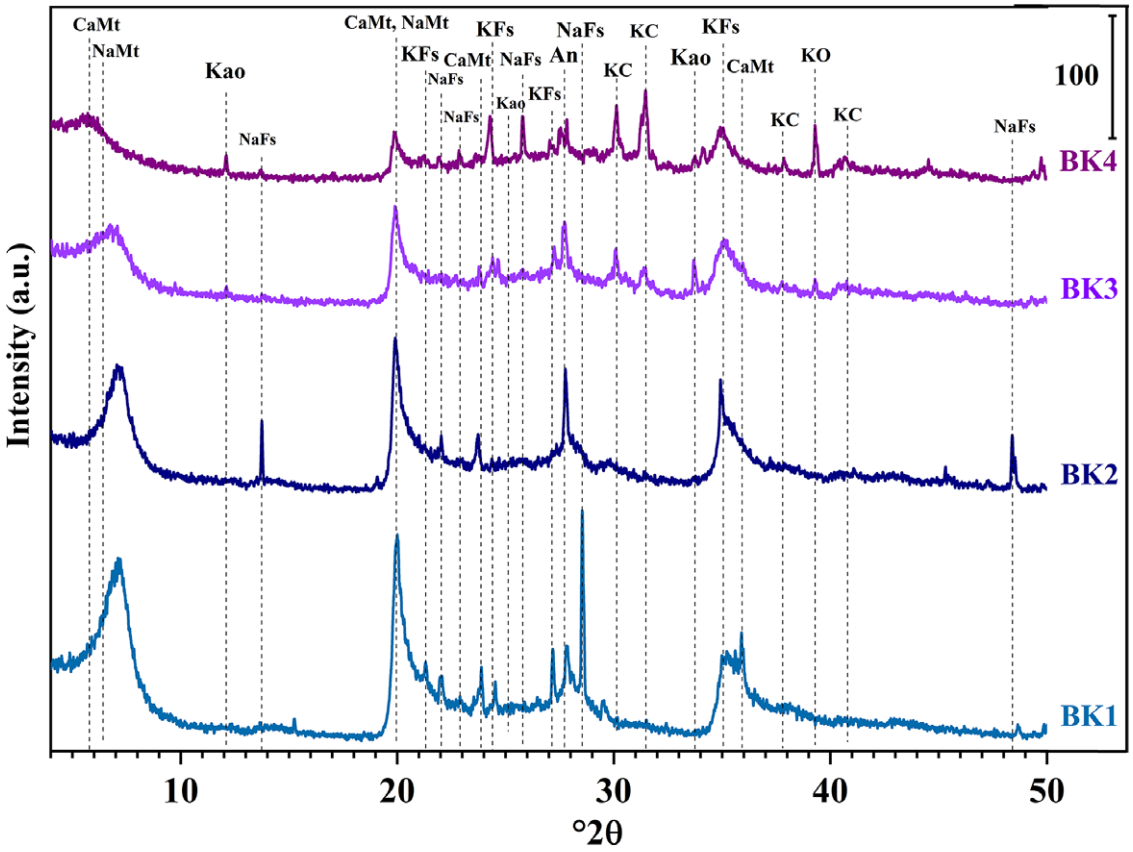

Figure 5. XRD pattern of BK1, BK2, BK3, and BK4. CaMt = calcium montmorillonite; NaMt = sodium montmorillonite; An = anorthite; Kao = kaolinite; KFs = K-feldspar; NaFs = Na-feldspar; KO = hydrated potassium aluminium oxide; KC = potassium carbonate sesquihydrate.

Ca-montmorillonite and Na-montmorillonite peaks decreased in intensity and shifted toward small angles when 32 wt.% of KOH was added (Fig. 5). KOH solution induced a mineralogical change in the 2:1 layer of montmorillonite that increased the layer charge by increasing the Al content (Bauer et al., 2006).

A small peak, characteristic of kaolinite, appeared at 7.32 Å for BK3 and BK4 (Fig. 5). The Si/Al molar ratio was, on average, equal to 0.5 for montmorillonite, and 1 for kaolinite. The progressive loss of the tetrahedral sheets in montmorillonite layers and the increase in hydroxyl content at the surface of the exposed octahedral sheet transformed smectite into kaolinite in highly alkaline conditions (pH >14) according to the following reaction (Eqn 4; Dudek et al., 2006):

$$\text{Smectite} + Si^{4+} \rightarrow \text{kaolinite} \quad (4)$$

Montmorillonite transformed into kaolinite and silica according to the following reaction (Eqn 5; Altschuler et al., 1963):

$$\text{Montmorillonite} \rightarrow \text{kaolinite} + \text{silica} \quad (5)$$

With the addition of KOH, potassium carbonate sesquihydrate ($K_2CO_3 \cdot 1.5H_2O$) and potassium aluminum oxide hydrate ($K_2Al_2O_4\ 3H_2O$) appeared in BK3 and BK4 (Fig. 5). Potassium carbonate sesquihydrate formed during the synthesis of C-S-H gel in a 1.0 M KOH solution (Yan et al., 2022). Potassium aluminum oxide hydrate was obtained following the attack on alumina by KOH (Zhang et al., 2008).

The presence of minor phases in bentonite, such as feldspars and anorthite, did not affect the reactivity of natural montmorillonite with the various bases. These aluminosilicates seem to be unaltered under hyperalkaline conditions, as evidenced by their clear detection by XRD (Figs 2–5).

Evolution of the d_{001} reflection of Ca/Na-montmorillonite

The system studied was quite complex with several clay mineral phases undergoing dissolution. Dissolution-precipitation reactions could be dominant, leading to a broadening of the diffraction peaks due to the decrease in particle size. Several processes together lead to these changes, therefore the discussion related to the differences in cation hydration might account for part of the material, but not all of the processes.

The intensity of the montmorillonite peak in the XRD patterns (Fig. 6) decreased as the quantity of CaO increased. This could be attributed to the dilution of montmorillonite by the lime present in the sample or more significantly to its dissolution. The montmorillonite peak became flattened, shifting toward the peak of Ca-montmorillonite, while the Na-montmorillonite peak disappeared.

The addition of MgO did not show any change in the d_{001} position, but its intensity decreased with increasing the amount of MgO added (Fig. 6). The basal spacing (d_{001}) is governed by the size and the degree of hydration. The basal spacings of non-hydrated montmorillonite exchanged with small cations Mg^{2+} and Ca^{2+} are similar (Berghout et al., 2010). The decrease in peak intensity could be attributed to the dissolution of the counter cations in montmorillonite under alkaline conditions (pH=11.4).

https://doi.org/10.1017/cmn.2024.27 Published online by Cambridge University Press

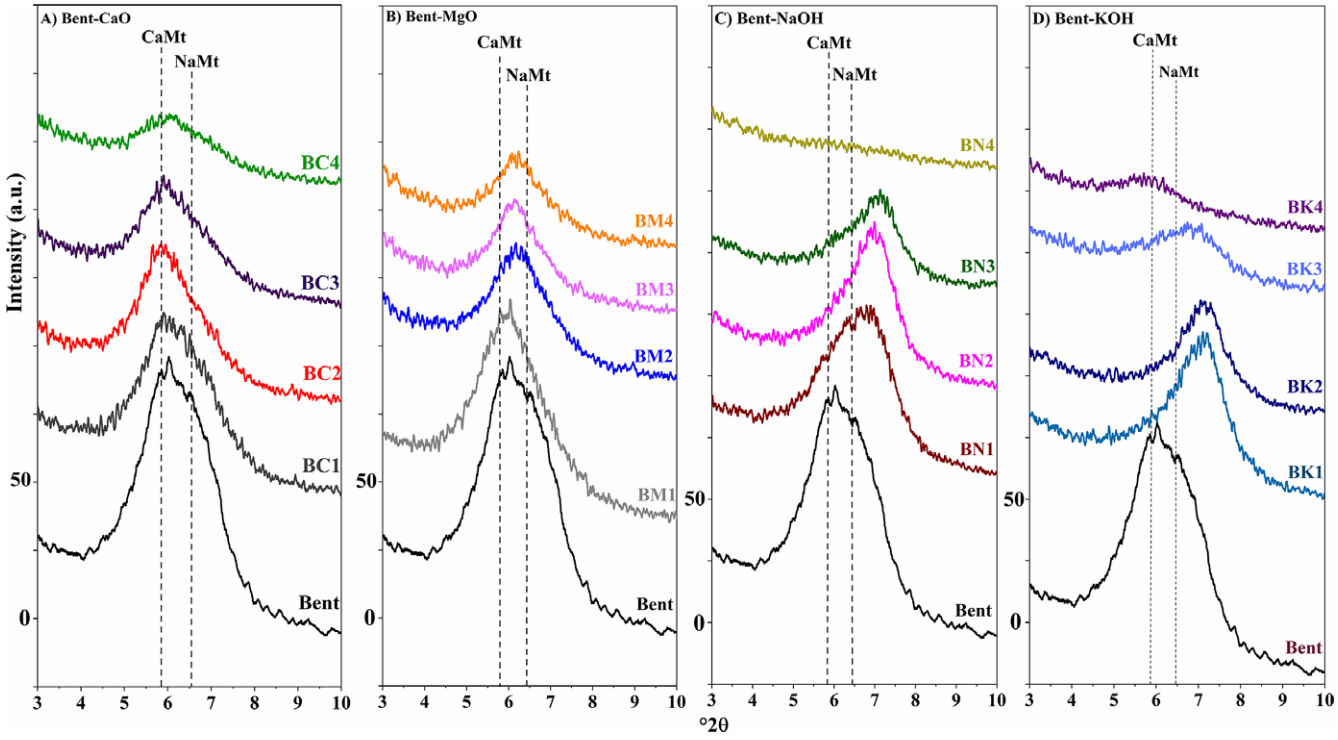

Figure 6. Evolution of the position of the (001) peak of montmorillonite.

With the addition of NaOH, the characteristic peak of montmorillonite flattened and decreased in intensity with increasing amount of NaOH added. Extreme sodification of montmorillonite was observed. With the addition of 2–8 wt.% of KOH (BK1 and BK2), the intensity of the montmorillonite peak decreased and moved toward high angles (2θ ~7). This decrease in the d_{001} value could be due to the ionic radius of K^+ (133 pm), which makes it difficult to penetrate the cavities of the tetrahedral sheets (Bray and Redfern, 2000), causing shrinkage (Watanabe and Yokoyama, 2022). When large amounts of KOH (16–32 wt.%, BK3 and BK4 specimens) were added, the (001) peak of montmorillonite became broad and an expansion of the interlayer space was observed. Sodium-montmorillonite saturated with Na^+ and K^+ have larger (decrease in 2θ) d-spacings and broader reflections than Na-montmorillonite saturated with Ca^{2+} or Mg^{2+} (Bray and Redfern, 2000; Titiloye and Skipper, 2005). This could indicate that Na^+ and K^+ have lower hydration energies than Ca^{2+} or Mg^{2+} (Rao et al., 2008) and lower hydrated radius (Nightingale, 1959; Volkov et al., 1997):

$$\Delta H_{(K(H2O)+)}\left(69.7\,kJ\,mol^{-1}\right) < \Delta H_{(Na(H2O)+)}\left(102\,kJ\,mol^{-1}\right)$$
$$< \Delta H_{(Ca(H2O)2+)}\left(220.1\,kJ\,mol^{-1}\right) < \Delta H_{(Mg(H2O)2+)}\left(313.8\,kJ\,mol^{-1}\right)$$

$$R_{H(K(H2O)+)}\left(3.31\,^{\circ}\,A\right) < R_{H(Na(H2O)+)}\left(3.58\,^{\circ}\,A\right)$$
$$< R_{H(Ca(H2O)2+)}\left(4.12\,^{\circ}\,A\right) < R_{H(Mg(H2O)2+)}\left(4.28\,^{\circ}\,A\right)$$

The position of the Na^+ and K^+ interlayer cations was such that rehydration was possible. In contrast, Mg^{2+} and Ca^{2+} appeared to have penetrated the cavities of the outer tetrahedral sheets and could not readily form hydration spheres.

Infrared spectroscopy

FTIR was used to follow the modification of chemical composition of mortar specimens after 28 days of hydration (Table 3; Fig. 7).

FTIR spectra of raw bentonite showed a small band at 3698 cm^{-1} attributed to the -O–H stretch for Al-OH and Si-OH (Tabak et al., 2007). This absorption band persisted for BC2, BM2, BM4, BN2, and BK2, but disappeared for BC4, BN4, and BK4 when the structure of montmorillonite was strongly altered in a highly alkaline medium. In BM2 and BM4, the intensity of this absorption band increased due to the elongation vibration of the Mg–OH bond in brucite (Kloprogge et al., 1999). An absorption band was observed at 3620 cm^{-1} due to the elongation vibration of the O–H bond of the Al-O-H group of montmorillonites (Tabak et al., 2007) appearing in raw bentonite and specimens containing 8% oxides (CaO, MgO) or hydroxides (NaOH, KOH). When 32% oxides or hydroxides was added, this absorption band weakened for BC4, BM4, and BK4, and disappeared for BN4. This decrease could be attributed to the destabilization of the structure of montmorillonite. A broad absorption band was observed at ~3423 cm^{-1} corresponding to the vibration of OH bond of the C-S-H gel (Chukanov, 2013) or to the O–H stretching vibrations of water physisorbed on the surface of matter (Tabak et al., 2007). An absorption band at 1639 cm^{-1} is attributed to the H-O-H-bending vibrations of H_2O (Zhang et al., 2020). This absorption band disappeared or increased in size when the quantity of oxides or hydroxides increased.

A sharp absorption band appeared at 1436 cm^{-1} for BC, BN, and BK, associated with the bending vibration of C-O in CO_3^{2-} (Muraleedharan et al., 2021). The intensity of this band increased with CaO and KOH added to bentonite. This may be due to the formation of calcite in BC and potassium carbonate in BK specimens as confirmed by XRD. Monocarboaluminate was only

https://doi.org/10.1017/cmn.2024.27 Published online by Cambridge University Press

Table 3. Absorption bands from FTIR spectra of bentonite, BC2, BC4, BM2, BM4, BN2, BN4, BK2, and BK4

Band (cm^{-1})	B	BC2	BC4	BM2	BM4	BN2	BN4	BK2	BK4	Assignment
3698	L	L	—	I	I	L	—	L	—	Al(Mg)–O–H stretching of montmorillonite (Patel et al., 2006; Tabak et al., 2007) Mg–O–H stretching of brucite (Kloprogge et al., 1999)
3620	I	I	L	I	L	I	—	I	L	Smectite OH stretch (Patel et al., 2006)
3423	—	I	LL	I	LL	I	LL	I	LL	H–O–H for H_2O (Tabak et al., 2007; Zhang et al., 2020)
1639	I	I	L	I	L	I	LL	I	I	–OH bending hydration (Patel et al., 2006; Shiferaw et al., 2019; Zhang et al., 2020)
1436, 1403	—	L	I	LL	LL	I	I	I	I	CO_3 stretching of calcite (Tabak et al., 2007)
1115	I	I	I	I	I	I	—	I	I	Si–O stretching (Patel et al., 2006; Tabak et al., 2007)
996	I	I	I	I	I	I	I	I	I	Si–O–Si stretching (Patel et al., 2006; Tabak et al., 2007)
907	I	I	I	I	I	I	I	I	I	OH bending bounded $2Al^{+3}$ (Patel et al., 2006; Tabak et al., 2007)
870	—	—	I	—	—	—	—	—	—	v2 Asymmetric CO_3 stretching (Shiferaw et al., 2019)
862	—	—	—	—	—	L	I	—	—	Bending bands of carbonate groups of cancrinite
825	—	—	—	—	—	—	—	—	I	Tetrahedrally coordinated Al atom in $K_2Al_2O_4.3H_2O$ (Padmaja et al., 2001; Lakhno et al., 2012)
698	I	L	I	L	L	L	L	L	I	Si–O stretching and the in–plane bending of calcite (Tabak et al., 2007)
520	I	L	L	L	L	L	LL	L	L	Al–Si–O bending (Patel et al., 2006; Tabak et al., 2007)

L = low; I = intense; LL = low and large.

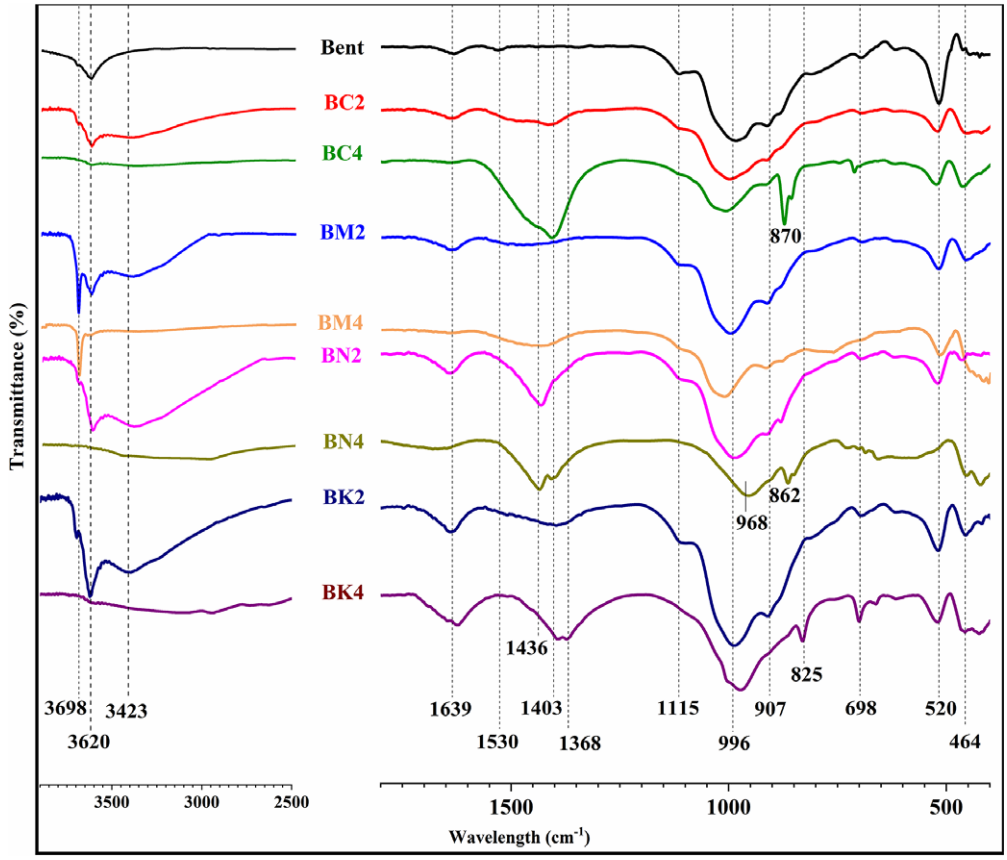

Figure 7. FTIR spectra of BC2, BC4, BM2, BM4, BN2, BN4, BK2, and BK4.

https://doi.org/10.1017/cmn.2024.27 Published online by Cambridge University Press

Table 4. DTA/TGA results of raw bentonite, BC2, BC4, BM2, BM4, BN2, BN4, BK2, and BK4

	Temperature (°C)	Bentonite		BC2	BC4	BM2	BM4	BN2	BN4	BK2	BK4
TGA	25–250	Weight loss (%)	12	7.9	7.2	6.7	5.4	10.1	14.2	7.6	11.4
		Assignment	Dehydration								
	250–550	Weight loss (%)	3.3	4.2	4.2	5.1	13.0	3.3	6.4	4.1	4.1
		Assignment	Dehydroxylation								
	550–1000	Weight loss (%)	2.3	7.9	17.6	1.5	2.2	0.3	4.2	1.2	5.8
		Assignment	Dehydroxylation and decarbonation								
	25–1000	Total weight loss (%)	17.5	17	28.3	13. 3	20.6	13.7	24.8	12.9	21.3
		Total bentonite loss (%)	17.5	27.0	60.7	21.1	44.2	21.7	53.2	20.5	45.7
		Bentontite contribution (%)	100	64.9	28.8	82.9	39.6	80.5	32.9	85.5	38.7
DTA	96 (average)	Endothermic peak	80 (I)	107 (I)	96 (I)	98 (I)	90 (I)	96 (I)	114 (I)	96 (I)	92 (I)
		Assignment	Dehydration of water physisorbed[a]								
	173	Endothermic peak		177 (L)	178 (L)					160 (L)	177 (I)
		Assignment	Dehydration of water physisorbed[a]								
			Dehydration of interlayer water for BC[b]								
			Dehydration of $K_2CO_3 \cdot 1.5H_2O$ for BK[c]								
	410	Endothermic peak					411 (I)				
		Assignment	Dihydroxylation of brucite[d]								
	470	Endothermic peak			473 (M)					469 (L)	
		Assignment	Dihydroxylation of portlandite[e]								
	500	Endothermic peak	509 (M)	494 (M)		498 (M)	511 (L)	498 (M)			–
		Assignment	Dehydroxylation of Ca–montmorillonite[f]								
	660	Endothermic peak	662 (M)	654 (M)	674 (L)				675 (M)	628 (M)	
		Assignment	Dihydroxylation of Ca–montmorillonite[f]								
	780	Endothermic peak									
		Assignment	Decomposition of calcite[g]								
	892	Endothermic peak							892 (M)		
		Assignment	Decarbonation cancrinite[h]								

L = low; M = medium; I = intense.
[a]Bounab et al., (2017);
[b]Ikari et al., (2007);
[c]Duan et al., (2012);
[d]Nied et al., (2016);
[e]Chhaiba et al., (2018);
[f]Caglar et al., (2009);
[g]Wang et al., (2018);
[h]Dumańska-Słowik et al., (2016).

observed in BC4 highlighted by the split ν3-CO_3^{2-} at 1403 cm^{-1} and ν2-CO_3^{2-} at 870 cm^{-1} (Shiferaw et al., 2019). An absorption band was observed at 1115 cm^{-1} in all samples expect in BN4, attributed to the Si-O stretching of montmorillonite (Tabak et al., 2007). A broad absorption band situated at 996 cm^{-1} attributed to Si-O-Si stretching was observed in all samples with a slight displacement at 956 cm^{-1} for BN4 (Tabak et al., 2007). This displacement could be attributed to the formation of sodalite and cancrinite. A broad absorption band was observed at 979 cm^{-1} attributed to vibrational frequencies of (Si, Al)-O bond in tetrahedron $[(Si,Al)O_4]^{4-}$ of hydrosodalite (Vaičiukyniene et al., 2009). Absorption bands at 907, 698, and 520 cm^{-1} were observed in all samples, attributed to the Si-O stretching, OH bonded to $2Al^{3+}$ and Al-Si-O bending respectively (Tabak et al., 2007).

A narrow absorption band was observed at 870 cm^{-1} for BC4 specimen fits to ν2 asymmetric CO_3 stretching due to the formation of calcite (Shiferaw et al., 2019). The absorption band observed at 862 cm^{-1} for BN4 can be attributed to the bending bands of

https://doi.org/10.1017/cmn.2024.27 Published online by Cambridge University Press

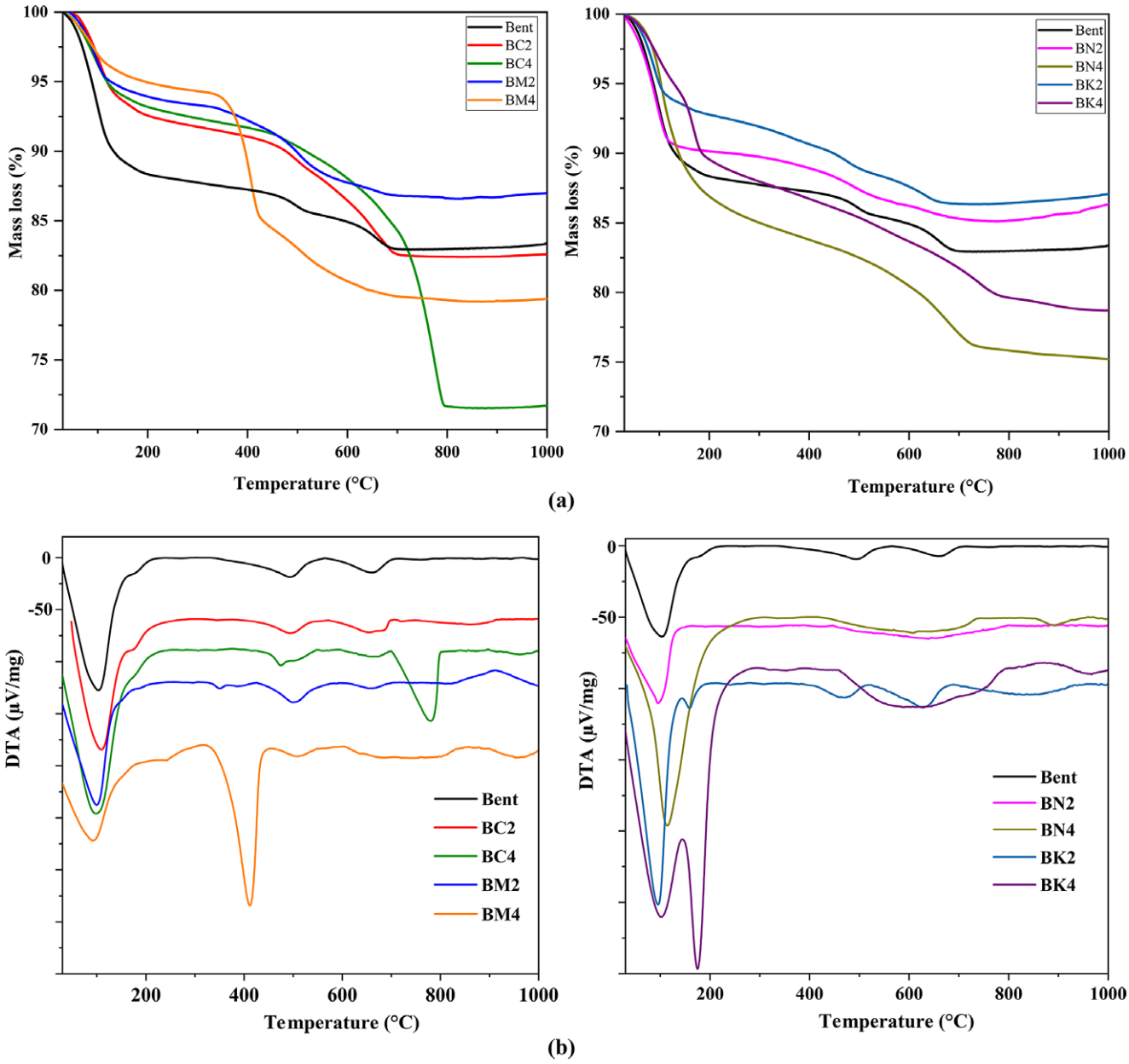

Figure 8. (a) TGA curves of raw bentonite (Bent) and mixtures BC2, BC4, BM2, BM4, BN2, BN4, BK2, and BK4; (b) DTA curves of raw bentonite (Bent) and mixtures BC2, BC4, BM2, BM4, BN2, BN4, BK2, and BK4.

carbonate groups of cancrinite (Rozenberg et al., 2009). An absorption band was observed at 825 cm^{-1} for BK4, indicating the increase in the tetrahedrally coordinated aluminum atom in $K_2Al_2O_4.3H_2O$ (Padmaja et al., 2001). It may also be because of Al-O out-of-plane vibration and reflects Al-for-Si substitution in the tetrahedral sheet (Xu et al., 2014).

Thermal characteristics

DTA/TGA results of raw bentonite and specimens made by oxides and hydroxides after 28 days of hydration indicated the occurrence of endothermic peaks associated with a loss of mass (Table 4; Fig. 8a,b). The weight loss between 25 and 250°C increased with increasing amount of CaO, NaOH, and KOH added to bentonite, but not MgO. This loss in weight was associated with two endothermic peaks at 107 and 172°C. The first peak was attributed to dehydration of water physisorbed on the grain surface of bentonite (Bounab et al., 2017) and the second is due to dehydration of interlayer water of montmorillonite (Ikari et al., 2007). A small endothermic peak was observed at 172°C for BC2 and BC4 due to dehydration of the C-S-H gel (Li et al., 2018). This peak was intense for BK2 and BK4, attributed to dehydration to $K_2CO_3{\cdot}1.5H_2O$, which is stable up to 153° C at ambient atmosphere conditions, through the following phase transition reaction (Eqn 6):

$$K_2CO_3 \cdot 1.5H_2O \rightarrow K_2CO_3 + 1.5H_2O \quad (6)$$

https://doi.org/10.1017/cmn.2024.27 Published online by Cambridge University Press

Table 5. Chemical EDX-derived data of BC2, BC4, BM2, BM4, BN2, BN4, BK2, and BK4

	Al/Si	Ca/Si	Mg/Si	Na/Si	K/Si	Fe/Si
Bentonite	0.54	0.03	0.05	0.06	0.02	0.06
BC2	0.56	0.16	0.06	0.05	0.01	0.04
BC4	0.58	1.23	0.08	0.00	0.00	0.06
BM2	0.52	0.01	0.27	0.07	0.01	0.09
BM4	0.62	0.01	1.01	0.08	0.00	0.04
BN2	0.52	0.02	0.06	0.26	0.01	0.14
BN4	0.67	0.03	0.06	4.44	0.00	0.07
BK2	0.60	0.00	0.06	0.07	0.17	0.03
BK4	0.61	0.00	0.00	0.00	1.86	0.11

In the temperature range between 25 and 250°C, when CaO was added, loss of weight doubled from BC2 to BC4 due to dehydration of the C-S-H gel. For NaOH, the loss of mass was very important for BN2 and further increased for BN4, probably due to the departure of water molecules located in the channels and cages of the cancrinite and sodalite (Reyes et al., 2013). For KOH, the loss of weight increased from 7.61% to 11.3% for BK2 and BK4, respectively, due to dehydration of potassium carbonate sesquihydrate.

Slight and similar loss of mass (2–5%) was observed between 250 and 550°C, corresponding to the dehydroxylation of the phases formed, except for BM4 which was high (13%) due to the dehydroxylation of brucite. This loss of mass was associated with three endothermic peaks at 410, 475, and 509°C. The endothermic peak at 410°C was only observed in BM2 and BM4 with a highest intensity in BM4, attributed to the dehydroxylation of brucite (Nied et al., 2016). The second endothermic peak at 475°C was observed for BC2 and BC4, due to the dehydroxylation of portlandite (Chhaiba et al., 2018). A small endothermic peak at 509°C was observed for MC4 and BM4, corresponding to dehydroxylation of Ca-montmorillonite.

The third loss in weight occurred between 550 and 950°C, associated with three endothermic peaks at 509, 654, and 778°C. The peak at 509°C for raw bentonite, BC4, BM2, and BM4 is attributed to dehydroxylation of Ca-montmorillonite. The peak at 654°C was shown for all samples except for BN4 and BK4, due to the departure of structural water of Ca-montmorillonite (Xie et al., 2001). This peak can be attributed to the decarbonation of amorphous carbonate from the C-S-H gel formed for samples BC2 and BC4 (Bandipally et al., 2018). The peak at 778°C, only observed for BC4, is due to the loss of CO_2 of neoformed calcite (Wang et al., 2018).

Between 550 and 950°C, the loss in weight for BM2, BM4, BN2, and BK2 was small (1.3–2.4%) due to the dehydroxylation of Ca-montmorillonite. This small loss in weight could be attributed to the low amount of adsorbed water in the interfoliar space of montmorillonite as shown by XRD pattern for specimens mixed with NaOH and KOH (Fig. 6). For specimens mixed with MgO, brucite formation probably minimized the number of intercalated water molecules in the interfoliar space, while the loss in mass was around 5% for BC2, BN4, and BK4, and reached 17.6% for BC4. This slight increase in mass loss observed was probably due to decarbonation of cancrinite in BN4 (Kriaa et al., 2012), and to the dehydration of the formed $K_2CO_3{\cdot}1.5H_2O$ and $K_2Al_2O_4\,3H_2O$ in BK4.

The loss of total mass between 25 and 950°C increased with the increase in the amount added of CaO, MgO, NaOH, and KOH, indicating the formation of hydrates and carbonates. Bentonite represented 63% of total mass of specimens for BC2, BM2, BN2, and BK2, and 46.6% for BC4, BM4, BN4, and BK4 (10 g of the solid and 4.6 g of water, 8/14.6×100=63% or 32/14.6×100=46.6%). The calculation of the total loss in weight of bentonite in relation to the quantity of raw bentonite used to manufacture the specimens, allowed us to observe that losses came from other compounds (i.e. hydrates and calcareous phases). The contribution of bentonite to the loss (total loss of bentonite/16.8; 16.8 is the total mass loss of bentonite) decreased gradually as follows: BM2 ≈ BK2 <BN2 << BC2 and BM4 < BK4 <BN4 < BC4. Destabilization of bentonite structure occurs as follows: MgO < KOH << NaOH << CaO.

Microstructure

The SEM image of BC2 (Fig. 9a) showed a platelet morphology characteristic of smectites (González-Santamaría et al., 2021). Needle-shaped fibers formed in BC2 (Fig. 9a) with an average length of 4.34 µm. The EDX results of these needles showed 5.67% Ca, which could be attributed to the formation of aragonite, an unstable phase that subsequently transforms into the more stable calcite (Sharp et al., 2014; Karunarathne et al., 2019). The pozzolanic reaction developed from the surface of montmorillonite grains toward its inner part. The absence of portlandite and the presence of C-S-H gel as flakes confirmed the consumption of portlandite by pozzolanic reaction for BC2. The chemical compositions of these fibers indicated the presence of aluminum and calcium and the absence of sulfur (Table 5). Such morphology may affect the mechanical properties of the clayey paste by increasing cementation of the grains and decreasing their porosity and density.

The SEM image of the BC4 mixture showed a deposit of portlandite on montmorillonite grains; note that the alteration of the morphology of montmorillonite was not obvious. An excess of lime, visible on the outer surface of montmorillonite grains, may affect the mechanical strength of the BC4 mixture (Fig. 9, BC4). The SEM image of BM2 showed that montmorillonite grains were eroded at the surface (Fig. 9a, BM2). This could be explained by the formation of brucite on the surface of the grains. Brucite is subparallel to aggregates of plates in irregular form on the outer surface and the pores (Fernández et al., 2009). By adding 32% of MgO, a precipitation of nanocrystal in the outer surface of bentonite was observed. This precipitation may be due to an excess of periclase and brucite.

The external surface of the bentonite grains of sample BN4 was modified by the addition of NaOH. The morphology of montmorillonite was transformed into the typical texture of sodalite, as shown by XRD results (Fig. 9b, BN4). Sodalite nanocrystals agglomerate to form micro-granules with diameters of 8–500 nm (Khajavi et al., 2007). Montmorillonite treated with 5 M HCl and calcined for 4 h by hydrothermal pre-fusion gives sodalite (Belviso et al., 2017). The SEM images did not allow the observation of cancrinite grains.

SEM images of BK2 and BK4 showed that characteristic morphology of montmorillonite is well preserved despite the addition of KOH. An alteration of the outer surface of the montmorillonite grains was visible.

With the addition of CaO, the Ca/Si ratio increased from 0.16 to 1.23 for BC2 and BC4, respectively. The EDX results from SEM observations (Table 5) did not show any K and Na cations in the mixture BC4. This can be explained by the formation of C-S-H and C-A-H gels at the surface of bentonite and by the excess portlandite

https://doi.org/10.1017/cmn.2024.27 Published online by Cambridge University Press

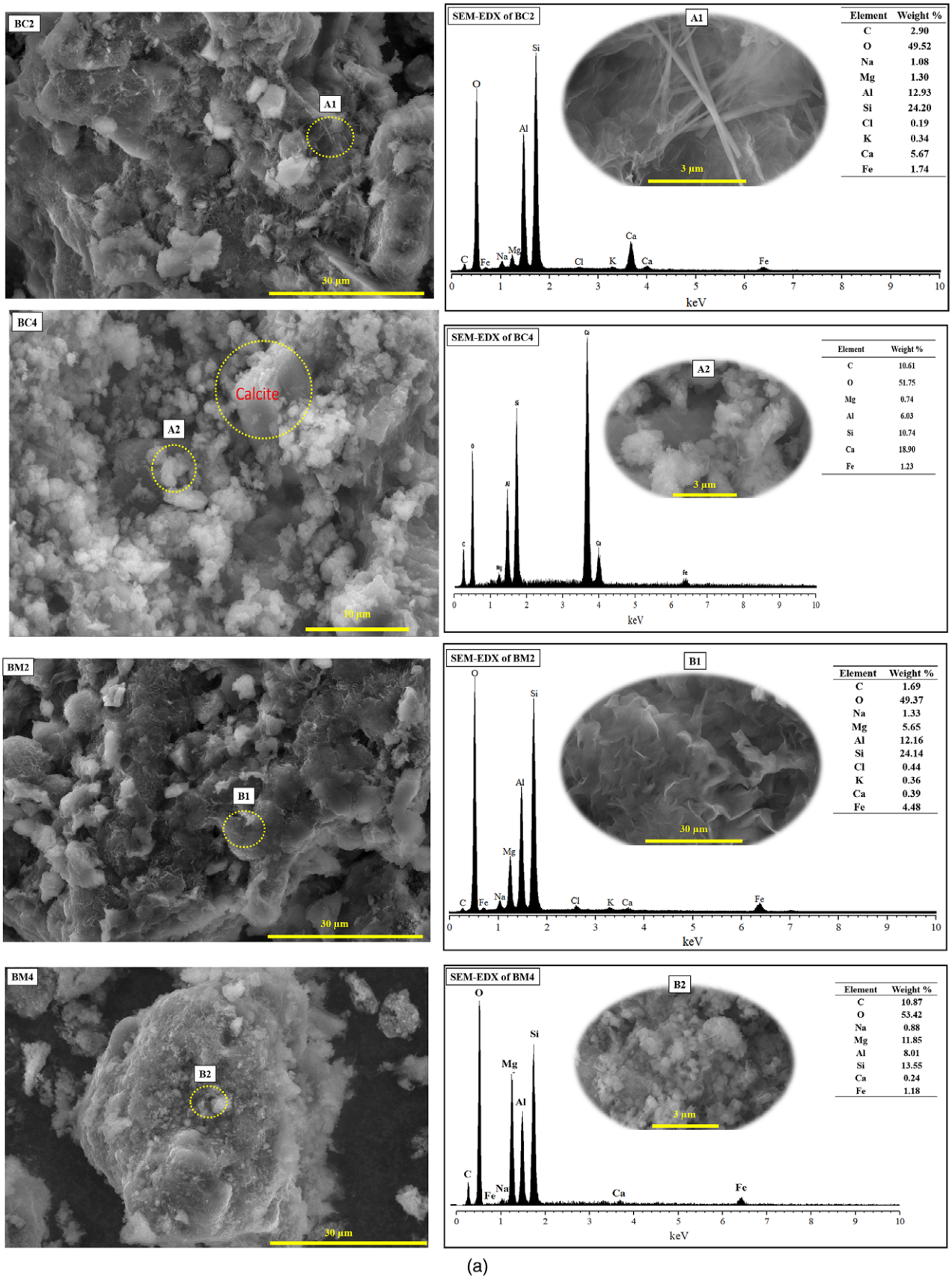

Figure 9. (a) SEM/EDX images of BC2, BC4, BM2, and BM4; (b) SEM/EDX images of BN2, BN4, BK2, and BK4.

https://doi.org/10.1017/cmn.2024.27 Published online by Cambridge University Press

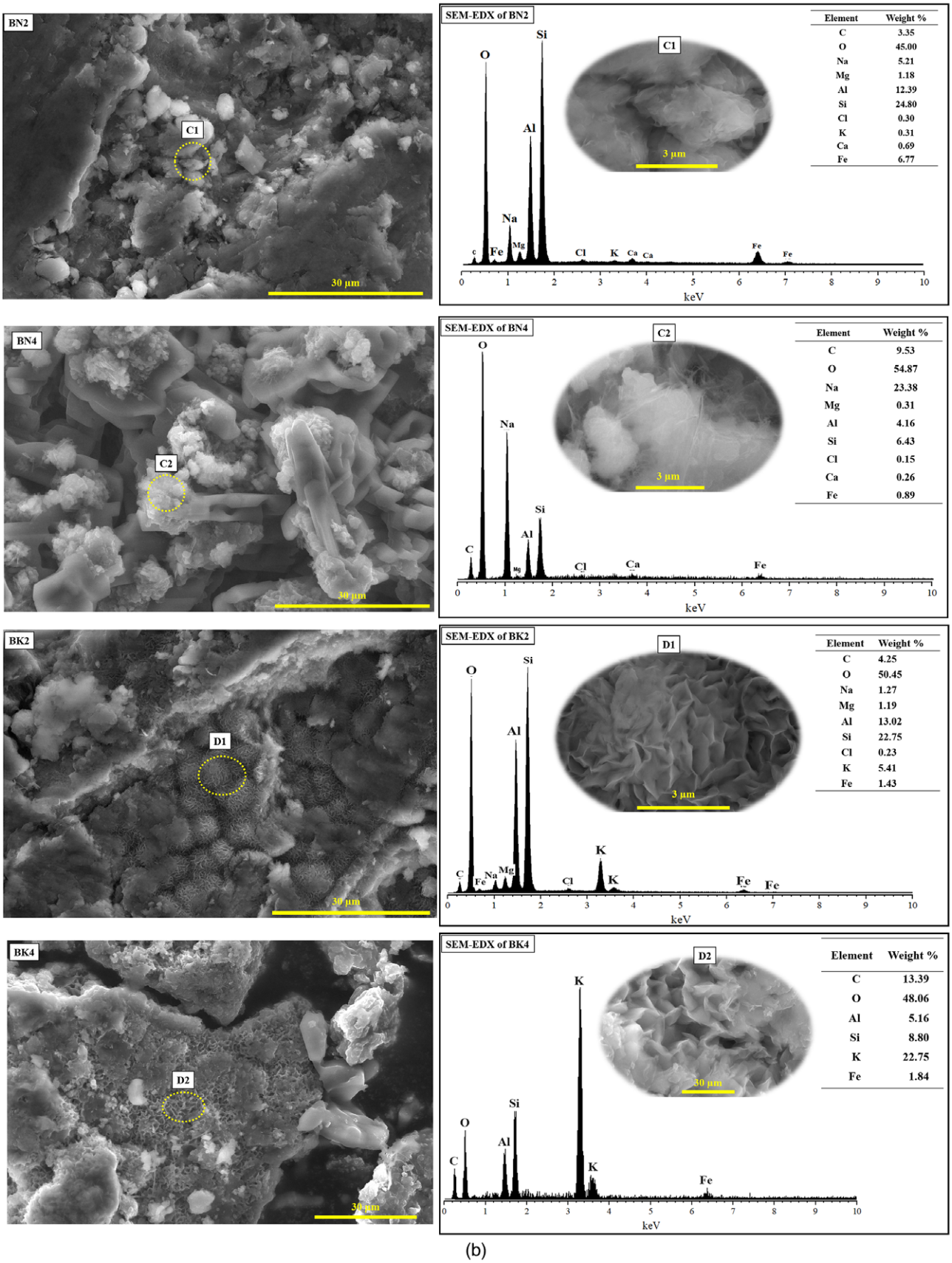

Figure 9. (Continued)

https://doi.org/10.1017/cmn.2024.27 Published online by Cambridge University Press

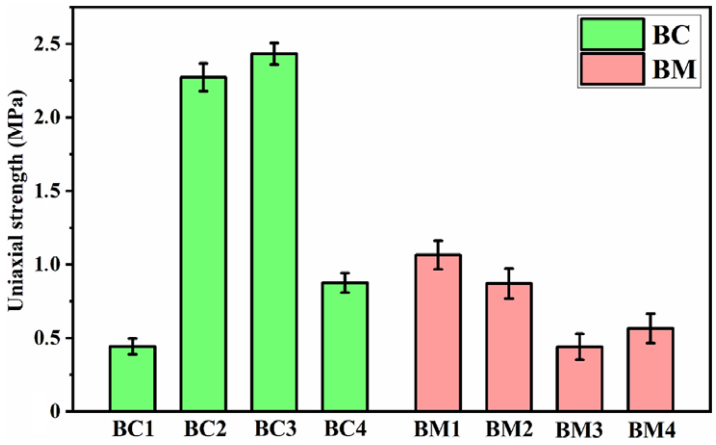

Figure 10. Uniaxial strength of bentonite-CaO (BC1–BC4) and bentonite-MgO (BM1–BM4) mixtures.

and calcite that precipitate on the outer area of bentonite. Likewise, with the addition of MgO, the Mg/Si ratio increased from 0.27 to 1.01 for BM2 and BM4, respectively, indicating the formation of periclase and brucite. The significant increase in Al/Si ratio of BN4 (0.67) compared to raw bentonite (Al/Si=0.54) is consistent with the formation of sodalite and cancrinite.

Mechanical behavior of bentonite in different alkaline environments

Testing the compressive strength of clay-based cementitious materials is crucial for assessing material strength, quality control, design decisions, and predicting structural longevity and durability. Bentonite-NaOH and bentonite-KOH specimens remained powdery without setting after 28 days due to the zeolitization of bentonite by NaOH and its transformation into kaolinite by KOH. Consequently, the compressive strength could not be measured for BN and BK. This lack of setting could be due to the absence of cementitious phase formation, influenced by the nature of the cation. There are several setting accelerators, such as chlorite and nitrate salts, that can be added to NaOH or KOH to allow the samples to set. The cation-accelerating strength of chloride and nitrate salts in the hydration of ordinary Portland cement, as observed in calorimetric experiments, follows this order (Wilding et al., 1984):

$$Ca^{2+} > Ni^{2+} > Ba^{2+} > Mg^{2+} > Fe^{3+} > Cr^{2+} > Co^{2+} > La^{3+} > > NH_4{}^+, K^+ > Li^+ > Na^+$$

However, in a hyperalkaline environment, a comprehensive study should be conducted, controlling other factors such as temperature, pH, and humidity, and choosing suitable accelerators.

Alkaline chlorides, such as sodium and potassium chloride, are not particularly effective at accelerating the setting and hardening of cement (Vehmas et al., 2018). Alkaline activation by sodium silicate, when applied to an aluminosilicate material, can dissolve silica and alumina in the soil (Muhammad and Siddiqua, 2022). This could potentially enhance the setting of BN and BK mixtures.

The uniaxial compression of bentonite-$Ca(OH)_2$ and bentonite-$Mg(OH)_2$ mixtures (Table 2) after 28 days of hydration (Fig. 10) increased with increasing lime content; it ranged from 0.44 MPa for BC1 (2% of CaO), to 2.27 MPa for BC2 (8% of CaO), to 2.47 MPa for BC3 (16% of CaO). This could be explained by the formation of C-S-H and C-A-H gel during the pozzolanic reaction. The longer the chains of C-S-H, the harder the clay paste became, which increased their compressive strength (Das et al., 2020). Ca^{2+} is the optimal accelerator for setting and hardening, which is why calcium salts (i.e. CaCl2 and $Ca(NO_3)_2$) are commonly used as accelerating admixtures in concrete (Dorn et al., 2022). The addition of 32% of CaO on raw bentonite decreased the compressive strength of the BC4 mixture to a value of 0.87 MPa due to the neoformation of calcite. The precipitation of calcite on bentonite grains prevented the development of silicate chains on the surface of bentonite grains; therefore, the C-S-H chains were short. Similarly, the compressive strength of the samples decreased with the addition of $Mg(OH)_2$. The dissolution of $Mg(OH)_2$ is slow, which does not favor the formation of M-S-H gel. The occurrence of $Mg(OH)_2$ after 30 days of hydration stabilized the microstructure of the cemented paste (Gonçalves et al., 2020), which could explain the setting of the clay.

Conclusions

The stability of raw bentonite from the Trebia deposit (Northeastern Morocco) in a very alkaline environment was investigated in the presence of various chemical species (CaO, MgO, NaOH, and KOH). The reaction mechanisms of montmorillonite with the different cations (Ca^{2+}, Mg^{2+}, Na^+, K^+) were highlighted. Our results showed that the addition of alkaline oxides or hydroxides affected the morphology of montmorillonite differently, and thus the mechanisms of pozzolanic reactions were different. This adds a new dimension to existing knowledge.

Our findings underscore the importance of the quantity added, the nature of the base, and the overall formulation of the concrete mixture. The addition of 8 wt.% of CaO destabilized montmorillonite and formed C-S-H gels and calcite. The addition of MgO did not affect the structure of montmorillonite and allowed the formation of brucite. The stabilized microstructure of the cemented paste and the setting of the clay were attributed to the formation of $Mg(OH)_2$ crystallites after 28 days of setting. As in the case of CaO, the compressive strength of the samples, although improving at low levels, decreases when the amount of MgO becomes very large. Mechanical strength was enhanced for bentonite-CaO mixtures more than bentonite-MgO mixtures.

https://doi.org/10.1017/cmn.2024.27 Published online by Cambridge University Press

The addition of 32 wt.% of NaOH caused the dissolution of montmorillonite and allowed the formation of sodalite and cancrinite. The addition of 32 wt.% of KOH to bentonite allowed the formation of kaolinite, potassium carbonate sesquihydrate, and potassium aluminum oxide hydrate. These findings diverge from those of Asano et al. (2008), who reported the conversion of Na-montmorillonite into Na-beidellite or Ca-montmorillonite in the presence of concentrated NaOH or $Ca(OH)_2$ solutions. A partial transformation of bentonite into kaolinite in KOH solutions was obtained at a temperature of 80°C (Ye et al., 2016).

Bentonite-NaOH and bentonite-KOH mixtures did not set due to the absence of the formation of gels and cementitious phases. Minor phases in bentonite such as feldspar and anorthite did not react with the four bases.

In sum, the incorporation of montmorillonite into concrete or road embankments is influenced by several factors. These include the quantity added, the nature of the montmorillonite, and the overall formulation of the concrete mix. Comprehensive testing and analysis are essential to evaluate the impact of adding montmorillonite on the properties of concrete.

Author contributions. Conceptualization: A. H., M. L., M. E., N. F., E. G.; A. H., E. G.; methodology, A. H., M. L., M. E., E. G.; experiments, A. H., M. L.; data analysis and interpretation, A. H., M. E., N. F., E. G.; writing, review and editing, A. H., M. L., M. E., N. F., E. G.

Acknowledgements. The authors would like to thank the Physical Measurements Platform of the Chemistry Department of Faculty of Sciences, Mohammed First University Oujda (Morocco). We are grateful to the National Center for Scientific and Technical Research for ICP-MS analysis.

Data availability statement. The data presented in this study are available on request from the corresponding author.

References

Altschuler, Z.S., Dwornik, E.J., & Kramer, H. (1963). Transformation of montmorillonite to kaolinite during weathering. *Science*, *141*(3576), 148–152. https://doi.org/10.1126/science.141.3576.148

Asano, T., Kawasaki, T., Higuchi, N., & Horikawa, Y. (2008). Feasibility study of solidification for low-level liquid waste generated by sulfuric acid elution treatment of spent ion exchange resin. *Journal of Power and Energy Systems*, *2*, 206–214. https://doi.org/10.1299/jpes.2.206

Baldermann, C., Baldermann, A., Furat, O., Krüger, M., Nachtnebel, M., Schroettner, H., Juhart, J., & Tritthart, J. (2019). Mineralogical and microstructural response of hydrated cement blends to leaching. *Construction and Building Materials*, *229*, 116902. https://doi.org/10.1016/j.conbuildmat.2019.116902

Bandipally, S., Cherian, C., & Arnepalli, D.N. (2018). Characterization of lime-treated bentonite using thermogravimetric analysis for assessing its short-term strength behaviour. *Indian Geotechnical Journal*, *48*, 393–404. https://doi.org/10.1007/s40098-018-0305-7

Bauer, A., Lanson, B., Ferrage, E., Emmerich, K., Taubald, H., Schild, D., & Veld, B. (2006). The fate of smectite in KOH solutions. *American Mineralogist*, *91*, 1313–1322. https://doi.org/10.2138/am.2006.2151

Belviso, C., Cavalcante, F., Niceforo, G., & Lettino, A. (2017). Sodalite, faujasite and A-type zeolite from 2:1dioctahedral and 2:1:1 trioctahedral clay minerals. A singular review of synthesis methods through laboratory trials at a low incubation temperature. *Powder Technology*, *320*, 483–497. https://doi.org/10.1016/j.powtec.2017.07.039

Berghout, A., Tunega, D., & Zaoui, A. (2010). Density functional theory (DFT) study of the hydration steps of $Na^+/Mg^{2+}/Ca^{2+}/Sr^{2+}/Ba^{2+}$-exchanged montmorillonites. *Clays and Clay Minerals*, *58*, 174–187. https://doi.org/10.1346/CCMN.2010.0580204

Bounab, L., Draoui, K., Ahrouch, M., Hadri, M., Bouchta, D., & Barhoun, A. (2017). An effective functionalized Moroccan bentonite: application for a green remediation of m-cresol. *Journal of Materials and Environmental Sciences*, *8*, 244–256.

Bray, H.J., & Redfern, S.A.T. (2000). Influence of counterion species on the dehydroxylation of Ca^{2+}-, Mg^{2+}-, Na^+-and K^+-exchanged Wyoming montmorillonite. *Mineralogical Magazine*, *64*, 337–346. https://doi.org/10.1180/002646100549238

Caglar, B., Afsin, B., Tabak, A., & Eren, E. (2009). Characterization of the cation-exchanged bentonites by XRPD, ATR, DTA/TG analyses and BET measurement. *Chemical Engineering Journal*, *149*, 242–248. https://doi.org/10.1016/j.cej.2008.10.028

Chhaiba, S., Blanco-Varela, M.T., Diouri, A., & Bougarrani, S. (2018). Characterization and hydration of cements and pastes obtained from raw mix containing Moroccan oil shale and coal waste as a raw material. *Construction and Building Materials*, *189*, 539–549. https://doi.org/10.1016/j.conbuildmat.2018.09.014

Christidis, G.E. (ed) (2011). *Advances in the Characterization of Industrial Minerals* (Vol. *9*). EMU Notes in Mineralogy, The European Mineralogical Union and The Mineralogical Society of Great Britain and Ireland.

Chukanov, N.V. (2013). *Infrared Spectra of Mineral Species: Extended Library*. Springer Science & Business Media.

Das, S., Ray, S., & Sarkar, S. (2020). Early strength development in concrete using preformed CSH nano crystals. *Construction and Building Materials*, *233*, 117214. https://doi.org/10.1016/j.conbuildmat.2019.117214

Daou, I., Zegaoui, O., Chfaira, R., Ahlafi, H., & Moussout, H. (2015). Physico-chemical characterization and kinetic study of methylene blue adsorption onto a Moroccan Bentonite. *International Journal of Science and Research*, *5*, 293–301.

Dodds, P.C., Williams, G., & Radcliffe, J. (2017). Chromate-free smart release corrosion inhibitive pigments containing cations. *Progress in Organic Coatings*, *102*, 107–114. https://doi.org/10.1016/j.porgcoat.2016.05.005

Dorn, T., Blask, O., & Stephan, D. (2022). Acceleration of cement hydration – a review of the working mechanisms, effects on setting time, and compressive strength development of accelerating admixtures. *Construction and Building Materials*, *323*, 126554. https://doi.org/10.1016/j.conbuildmat.2022.126554

Duan, Y., Luebke, D.R., Pennline, H.W., Li, B., Janik, M.J., & Halley, J.W. (2012). Ab initio thermodynamic study of the CO_2 capture properties of potassium carbonate sesquihydrate, K_2CO_3 1.5 H_2O. *Journal of Physical Chemistry C*, *116*, 14461–14470. https://doi.org/10.1021/jp303844t

Dudek, T., Cuadros, J., & Fiore, S. (2006). Interstratified kaolinite-smectite: nature of the layers and mechanism of smectite kaolinization. *American Mineralogist*, *91*, 159–170. https://doi.org/10.2138/am.2006.1897

Dumańska-Słowik, M., Pieczka, A., Heflik, W., & Sikorska, M. (2016). Cancrinite from nepheline syenite (mariupolite) of the Oktiabrski massif, SE Ukraine, and its growth history. *Spectrochimica Acta Part A: Molecular and Biomolecular Spectroscopy*, *157*, 211–219. https://doi.org/10.1016/j.saa.2016.01.007

El Bouraie, M., & Masoud, A.A. (2017). Adsorption of phosphate ions from aqueous solution by modified bentonite with magnesium hydroxide Mg $(OH)_2$. *Applied Clay Science*, *140*, 157–164. https://doi.org/10.1016/j.clay.2017.01.021

Elert, K., Pardo, E.S., & Rodriguez-Navarro, C. (2015). Mineralogical evolution of di-and trioctahedral smectites in highly alkaline environments. *Clays and Clay Minerals*, *63*, 414–431. https://doi.org/10.1346/CCMN.2015.0630601

Fayoyiwa, A.D., Hirvi, J.T., & Pakkanen, T.A. (2020). Roles of alkaline-earth cation species in the swelling pressure of smectites–A computational study. *Chemical Physics Letters*, *753*, 137602. https://doi.org/10.1016/j.cplett.2020.137602

Fernández, R., Mäder, U.K., Rodríguez, M., Vigil De La Villa, R., & Cuevas, J. (2009). Alteration of compacted bentonite by diffusion of highly alkaline solutions. *European Journal of Mineralogy*, *21*, 725–735. https://doi.org/10.1127/0935-1221/2009/0021-1947

Fernández, R., Ruiz, A.I., & Cuevas, J. (2014). The role of smectite composition on the hyperalkaline alteration of bentonite. *Applied Clay Science*, *95*, 83–94. https://doi.org/10.1016/j.clay.2014.03.015

Gautier, M., Muller, F., Le Forestier, L., Beny, J.M., & Guégan, R. (2010). NH_4-smectite: characterization, hydration properties and hydro mechanical behaviour. *Applied Clay Science*, *49*, 247–254. https://doi.org/10.1016/j.clay.2010.05.013

Gonçalves, T., Silva, R.V., De Brito, J., Fernández, J.M., & Esquinas, A.R. (2020). Mechanical and durability performance of mortars with fine recycled concrete aggregates and reactive magnesium oxide as partial cement replacement. *Cement and Concrete Composites*, *105*, 103420. https://doi.org/10.1016/j.cemconcomp.2019.103420

González-Santamaría, D.E., Justel, A., Fernández, R., Ruiz, A.I., Stavropoulou, A., Rodríguez-Blanco, J.D., & Cuevas, J. (2021). SEM-EDX study of bentonite alteration under the influence of cement alkaline solutions. *Applied Clay Science*, *212*, 106223. https://doi.org/10.1016/j.clay.2021.106223

Hackbarth, K., Gesing, T.M., Fechtelkord, M., Stief, F., & Buhl, J.C. (1999). Synthesis and crystal structure of carbonate cancrinite Na_8 $[AlSiO_4]$ $6CO_3$ $(H_2O)_{3.4}$, grown under low-temperature hydrothermal conditions. *Microporous and Mesoporous Materials*, *30*, 347–358. https://doi.org/10.1016/S1387-1811(99)00046-3

Harrou, A., Gharibi, E.K., Taha, Y., Fagel, N., & El Ouahabi, M. (2020). Phosphogypsum and black steel slag as additives for ecological bentonite-based materials: microstructure and characterization. *Minerals*, *10*, 1067. https://doi.org/10.3390/min10121067

Huang, Y., & Zhang, Z. (2023). Ion exchange selectivity (Mg^{2+}, Ca^{2+} and K+) in hydrated Na-montmorillonite: insights from molecular dynamic simulations. *Molecular Simulation*, *49*, 223–232. https://doi.org/10.1080/08927022.2022.2152062

Ikari, M.J., Saffer, D.M., & Marone, C. (2007). Effect of hydration state on the frictional properties of montmorillonite-based fault gouge. *Journal of Geophysical Research: Solid Earth*, *112*. https://doi.org/10.1029/2006JB004748

Jing, Z., Hao, W., He, X., Fan, J., Zhang, Y., Miao, J., & Jin, F. (2016). A novel hydrothermal method to convert incineration ash into pollucite for the immobilization of a simulant radioactive cesium. *Journal of Hazardous Materials*, *306*, 220–229. https://doi.org/10.1016/j.jhazmat.2015.12.024

Karunarathne, V.K., Paul, S.C., & Šavija, B. (2019). Development of nano-SiO_2 and bentonite-based mortars for corrosion protection of reinforcing steel. *Materials*, *12*, 2622. https://doi.org/10.3390/ma12162622

Khajavi, S., Kapteijn, F., & Jansen, J.C. (2007). Synthesis of thin defect-free hydroxy sodalite membranes: new candidate for activated water permeation. *Journal of Membrane Science*, *299*, 63–72. https://doi.org/10.1016/j.memsci.2007.04.027

Khalifa, A.Z., Cizer, Ö., Pontikes, Y., Heath, A., Patureau, P., Bernal, S.A., & Marsh, A.T. (2020). Advances in alkali-activation of clay minerals. *Cement and Concrete Research*, *132*, 106050.

Kloprogge, J.T., & Frost, R.L. (1999). Fourier transform infrared and Raman spectroscopic study of the local structure of Mg-, Ni-, and Co-hydrotalcites. *Journal of Solid State Chemistry*, *146*, 506–515. https://doi.org/10.1006/jssc.1999.8413

Kriaa, A., Ben Saad, K., & Hamzaoui, A.H. (2012). Synthesis and characterization of cancrinite-type zeolite, and its ionic conductivity study by AC impedance analysis. *Russian Journal of Physical Chemistry A*, *86*, 2024–2032. https://doi.org/10.1134/S0036024412130158

Lakhno, E.I., Burmakin, E.I., Korzun, I.V., & Shekhtman, G.S. (2012). Ion-electron transfer in solid solutions Rb(2−2x)Fe(2−x)PxO4. *Physics of the Solid State*, *54*, 504–507. https://doi.org/10.1134/S106378341203016X

Li, W., Yu, J., Ma, S., Hu, Y., Ge, D., & Shen, X. (2018). The properties and hydration of Portland cement containing calcium sulfoaluminate cement. *Ceramics Silikáty*, *62*, 364–373. https://doi.org/10.13168/cs.2018.0032

Likos, W.J., & Lu, N. (2006). Pore-scale analysis of bulk volume change from crystalline interlayer swelling in Na^+-and Ca^{2+}-smectite. *Clays and Clay Minerals*, *54*, 515–528. https://doi.org/10.1346/CCMN.2006.0540412

Liu, B., Sun, H., Peng, T., & He, Q. (2018). One-step synthesis of hydroxysodalite using natural bentonite at moderate temperatures. *Minerals*, *8*, 521. https://doi.org/10.3390/min8110521

Lothenbach, B., Nied, D., L'Hôpital, E., Achiedo, G., & Dauzères, A. (2015). Magnesium and calcium silicate hydrates. *Cement and Concrete Research*, *77*, 60–68. https://doi.org/10.1016/j.cemconres.2015.06.007

MacKenzie, K.J. (2009). Utilisation of non-thermally activated clays in the production of geopolymers. In *Geopolymers* (pp. 294–314). Woodhead Publishing.

Marsh, A., Heath, A., Patureau, P., Evernden, M., & Walker, P. (2019). Phase formation behaviour in alkali activation of clay mixtures. *Applied Clay Science*, *175*, 10–21.

Muhammad, N., & Siddiqua, S. (2022). Calcium bentonite vs sodium bentonite: the potential of calcium bentonite for soil foundation. *Materials Today: Proceedings*, *48*, 822–827. https://doi.org/10.1016/j.matpr.2021.02.386

Muraleedharan, M.G., Asgar, H., Hahn, S.H., Dasgupta, N., Gadikota, G., & Van Duin, A.C. (2021). Interfacial reactivity and speciation emerging from Na-montmorillonite interactions with water and formic acid at 200C: insights from reactive molecular dynamics simulations, infrared spectroscopy, and X-ray scattering measurements. *ACS Earth and Space Chemistry*, *5*, 1006–1019. https://doi.org/10.1021/acsearthspacechem.0c00286

Murray, H.H. (2000). Traditional and new applications for kaolin, smectite, and palygorskite: a general overview. *Applied Clay Science*, *17*, 207–221. https://doi.org/10.1016/S0169-1317(00)00016-8

Murray, H.H. (2006). Bentonite applications. In *Developments in Clay Science 2* (pp. 111–130). Elsevier. https://doi.org/10.1016/S1572-4352(06)02006-X

Nickovic, S., Vukovic, A., Vujadinovic, M., Djurdjevic, V., & Pejanovic, G. (2012). High-resolution mineralogical database of dust-productive soils for atmospheric dust modeling. *Atmospheric Chemistry and Physics*, *12*, 845–855. https://doi.org/10.5194/acp-12-845-2012

Nied, D., Enemark-Rasmussen, K., L'Hopital, E., Skibsted, J., & Lothenbach, B. (2016). Properties of magnesium silicate hydrates (MSH). *Cement and Concrete Research*, *79*, 323–332. https://doi.org/10.1016/j.cemconres.2015.10.003

Nightingale Jr, E.R. (1959). Phenomenological theory of ion solvation. Effective radii of hydrated ions. *Journal of Physical Chemistry*, *63*, 1381–1387. https://doi.org/10.1021/j150579a011

Oumnih, S., Bekkouch, N., Gharibi, E.K., Fagel, N., Elhamouti, K., & El Ouahabi, M. (2019). Phosphogypsum waste as additives to lime stabilization of bentonite. *Sustainable Environment Research*, *29*, 1–10. https://doi.org/10.1186/s42834-019-0038-z

Padmaja, P., Anilkumar, G.M., Mukundan, P., Aruldhas, G., & Warrier, K.G.K. (2001). Characterisation of stoichiometric sol–gel mullite by Fourier transform infrared spectroscopy. *International Journal of Inorganic Materials*, *3*, 693–698. https://doi.org/10.1016/S1466-6049(01)00189-1

Patel, H.A., Somani, R.S., Bajaj, H.C., & Jasra, R.V. (2006). Nanoclays for polymer nanocomposites, paints, inks, greases and cosmetics formulations, drug delivery vehicle and waste water treatment. *Bulletin of Materials Science*, *29*, 133–145. https://doi.org/10.1007/BF02704606

Provis, J.L. (2014). Geopolymers and other alkali activated materials: why, how, and what? *Materials and Structures*, *47*, 11–25.

Rao, J.S., Dinadayalane, T.C., Leszczynski, J., & Sastry, G.N. (2008). Comprehensive study on the solvation of mono-and divalent metal cations: Li+, Na+, K+, Be2+, Mg2+ and Ca2+. *The Journal of Physical Chemistry A*, *112*(50), 12944–12953. https://doi.org/10.1088/0953-8984/20/8/083202

Reyes, C.A.R., Williams, C., & Alarcón, O.M.C. (2013). Nucleation and growth process of sodalite and cancrinite from kaolinite-rich clay under low-temperature hydrothermal conditions. *Materials Research*, *16*, 424–438. https://doi.org/10.1590/S1516-14392013005000010

Rozenberg, K.A., Rastsvetaeva, R.K., & Chukanov, N.V. (2009). Crystal structures of oxalate-bearing cancrinite with an unusual arrangement of CO_3 groups and sulfate-rich davyne. *Crystallography Reports*, *54*, 793–799. https://doi.org/10.1134/S1063774509050101

Seo, S.M., Kim, D., Kim, D., Kim, J.H., Lee, Y.J., Roh, K.M., & Kang, I.M. (2018). A simple synthesis of nitrate cancrinite from natural bentonite. *Journal of Porous Materials*, *25*, 1561–1565. https://doi.org/10.1007/s10934-018-0569-4

Sharp, E.L., Al-Shehri, H., Horozov, T.S., Stoyanov, S.D., & Paunov, V.N. (2014). Adsorption of shape-anisotropic and porous particles at the air–water and the decane–water interface studied by the gel trapping technique. *RSC Advances*, *4*, 2205–2213. https://doi.org/10.1039/C3RA44563A

Shiferaw, N., Habte, L., Thenepalli, T., & Ahn, J.W. (2019). Effect of eggshell powder on the hydration of cement paste. *Materials*, *12*, 2483. https://doi.org/10.3390/ma12152483

Sun, W.J., Xu, G., Wei, G., Zhang, W.J., & Sun, D.A. (2021). Effects of ammonium ion and bentonite content on permeability of bentonite-clay mixture. *Environmental Earth Sciences*, *80*, 1–10. https://doi.org/10.1007/s12665-021-09440-w

https://doi.org/10.1017/cmn.2024.27 Published online by Cambridge University Press

Tabak, A., Afsin, B., Caglar, B., & Koksal, E. (2007). Characterization and pillaring of a Turkish bentonite (Resadiye). *Journal of Colloid and Interface Science*, *313*, 5–11. https://doi.org/10.1016/j.jcis.2007.02.086

Titiloye, J.O., & Skipper, N.T. (2005). Monte Carlo and molecular dynamics simulations of methane in potassium montmorillonite clay hydrates at elevated pressures and temperatures. *Journal of Colloid and Interface Science*, *282*, 422–427. https://doi.org/10.1016/j.jcis.2004.08.131

Tsipursky, S.I., & Drits, V.A. (1984). The distribution of octahedral cations in the 2:1 layers of dioctahedral smectites studied by oblique-texture electron diffraction. *Clay minerals*, *19*, 177–193. https://doi.org/10.1180/claymin.1984.019.2.05

Vaičiukyniene, D., Baltakys, K., & Kantautas, A. (2009). Hydrosodalite ion exchange in saturated Ca $(OH)_2$ solution. *Materials Science-Poland*, *27*, 417–426.

Vehmas, T., Kronlöf, A., & Cwirzen, A. (2018). Calcium chloride acceleration in ordinary Portland cement. *Magazine of Concrete Research*, *70*, 856–863. https://doi.org/10.1680/jmacr.17.00079

Vitale, E., Deneele, D., Paris, M., & Russo, G. (2017). Multi-scale analysis and time evolution of pozzolanic activity of lime treated clays. *Applied Clay Science*, *141*, 36–45. https://doi.org/10.1016/j.clay.2017.02.013

Volkov, A.G., Paula, S., & Deamer, D.W. (1997). Two mechanisms of permeation of small neutral molecules and hydrated ions across phospholipid bilayers. *Bioelectrochemistry and Bioenergetics*, *42*, 153–160. https://doi.org/10.1016/S0302-4598(96)05097-0

Wang, K., Ren, L., & Yang, L. (2018). Excellent carbonation behavior of rankinite prepared by calcining the CSH: potential recycling of waste concrete powders for prefabricated building products. *Materials*, *11*, 1474. https://doi.org/10.3390/ma11081474

Watanabe, Y., & Yokoyama, S. (2022). Effects of alteration on shear characteristics of compacted Ca-bentonite immersed in alkaline solutions. *Soils and Foundations*, *62*, 101199. https://doi.org/10.1016/j.sandf.2022.101199

Wilding, C.R., Walter, A., & Double, D.D. (1984). A classification of inorganic and organic admixtures by conduction calorimetry. *Cement and Concrete Research*, *14*, 185–194. https://doi.org/10.1016/0008-8846(84)90103-0

Xiang, G., Ye, W., Hu, Z., Ge, L., & Zhou, Y. (2022). Swelling characteristics of fractal-textured bentonite eroded by alkaline solution. *Advances in Civil Engineering*, *2022*. https://doi.org/10.1155/2022/9100822

Xiang, G., Ye, W., Yu, F., Wang, Y., & Fang, Y. (2019). Surface fractal dimension of bentonite affected by long-term corrosion in alkaline solution. *Applied Clay Science*, *175*, 94–101. https://doi.org/10.1016/j.clay.2019.04.010

Xie, W., Gao, Z., Liu, K., Pan, W. P., Vaia, R., Hunter, D., & Singh, A. (2001). Thermal characterization of organically modified montmorillonite. *Thermochimica Acta*, *367*, 339–350. https://doi.org/10.1016/S0040-6031(00)00690-0

Xu, B., Ding, S., & Cheng, H. (2014). The translation mechanism of smectite to illite: an infrared spectroscopic study of ordered mixed-layer illite/smecite. *Spectroscopy Letters*, *47*, 543–548. https://doi.org/10.1080/00387010.2013.821134

Yan, H., & Zhang, Z. (2021). Effect and mechanism of cation species on the gel properties of montmorillonite. *Colloids and Surfaces A: Physicochemical and Engineering Aspects*, *611*, 125824. https://doi.org/10.1016/j.cis.2007.12.008

Yan, Y., Yang, S.Y., Miron, G.D., Collings, I.E., L'Hôpital, E., Skibsted, J., Scrivener, K., & Lothenbach, B. (2022). Effect of alkali hydroxide on calcium silicate hydrate (CSH). *Cement and Concrete Research*, *151*, 106636. https://doi.org/10.1016/j.cemconres.2021.106636

Ye, W.M., He, Y., Chen, Y.G., Chen, B., & Cui, Y.J. (2016). Thermochemical effects on the smectite alteration of GMZ bentonite for deep geological repository. *Environmental Earth Sciences*, *75*, 1–11. https://doi.org/10.1007/s12665-016-5716-0

Zhang, W., Cheng, H., Peng, S., Li, D., Gao, H., & Wang, D. (2020). Performance and mechanisms of wastewater sludge conditioning with slag-based hydrotalcite-like minerals (Ca/Mg/Al-LDH). *Water Research*, *169*, 115265. https://doi.org/10.1016/j.watres.2019.115265

Zhang, Y., Zhang, Y., Xu, J., Jing, C., & Zhang, F. (2008). Studies of Al_2O_3–K catalysts prepared using various precursors for diesel soot elimination. *Thermochimica Acta*, *468*, 15–20. https://doi.org/10.1016/j.tca.2007.11.015

Zong, Y.B., Zhao, C.Y., Chen, W.H., Liu, Z.B., & Cang, D.Q. (2020). Preparation of hydro-sodalite from fly ash using a hydrothermal method with a submolten salt system and study of the phase transition process. *International Journal of Minerals, Metallurgy and Materials*, *27*, 55–62. https://doi.org/10.1007/s12613-019-1904-8

https://doi.org/10.1017/cmn.2024.27 Published online by Cambridge University Press